ARMA 15-755

Flow of high solid volume fraction fluids through fractures and around obstructions

Medina, R. and Detwiler, R. L.
University of California Irvine, Irvine, CA, USA
Prioul, R.[1], Morris J. P.[1,*], Ortega, J. A. [2], Desroches, J. [3]
Schlumberger, [1]Boston, MA, USA, [2]Sugar Land, TX, USA, and [3]Paris, France
**now at Lawrence Livermore National Laboratory, Livermore, CA, USA*

This paper was prepared for presentation at the 49th US Rock Mechanics / Geomechanics Symposium held in San Francisco, CA, USA, 28 June- 1 July 2015.

ABSTRACT: We present a set of experiments to investigate the development of solid volume fraction (ϕ) variations in the plane of a fracture in the direction perpendicular to the flow. We injected a concentrated suspension ($\phi = 0.5$) into the same parallel fracture in all the experiments, however, each experiment included one or two thin-plate obstructions at different locations and orientations within the fracture. Though the development of ϕ-gradients in the plane of the fracture was not observed in the experimental system, we did observed a surprising transient behavior of these concentrated suspensions. A pressure transient was observed at all flow rates in all experiments and suggests that the solid volume fraction distribution across the fracture as well as the distribution in the plane of the fracture affect the pressure response to a given flow rate. This pressure transient is related to the timescale associated with a solid distribution front reaching the fracture and can have major implications when designing experiments or interpreting pressure data from field operations.

1. INTRODUCTION

Flow of concentrated suspensions is important to a range of natural processes and engineered systems. Fluids from natural hazards (i.e. mud flows, avalanches, magma flows) are typically characterized by a large volume of suspended solids [1]. Industrial applications where suspended-solid flow is important include hydraulic fracturing for oil and gas production [2, 3], and environmental remediation [4]. The rheology, and flow behavior, of the carrier fluid is significantly different than the rheology of the suspension, which is strongly influenced by the solid volume fraction (ϕ). At high shear rates, the presence of the solids typically causes shear-thinning behavior, whereas at low shear rates, a yield stress is common [5]. This is especially important in confined geometries, i.e. fractures, tubes, etc., where the walls can exert large shear stresses.

For dilute suspensions ($\phi \lesssim 0.2$), the mixture behaves as a Newtonian fluid with viscosity that slowly increases with solid fraction [6]. In the concentrated regime, ϕ between ~0.2 and the random lose packing limit ($0.2 \lesssim \phi \lesssim \phi_{rlp}$), the apparent viscosity of the mixture increases significantly with increasing ϕ [7]. Above this value, in the dense regime the suspensions exhibit a yield stress as the solid content approaches a critical fluidity/jamming transition volume fraction (ϕ_{cr}) between the random lose packing limit and the random close packing limit ($\phi_{rlp} \lesssim \phi_{cr} \lesssim \phi_{rcp}$) [7]. If the solid concentration reaches a value above ϕ_{cr}, the suspension can support a finite shear stress, and thus exhibits properties of a solid [8]. At that point the suspended solids become immobilized and the suspension effectively becomes a porous medium with fluid moving through the particles. The suspension rheology is further complicated by the particle size distribution. Shapiro and Probstein [8] showed that fluids mixed with bimodal and multimodal sand distributions typically have lower viscosity than the same fluid mixed with monodisperse particle size distribution.

Previous studies of concentrated suspensions through confined geometries show that suspensions experience a shear induced particle migration towards the centerline of the geometry, i.e. away from the walls. This particle migration is induced by a combination of irreversible displacement due to interparticle interactions and shear stress gradients [9]. This migration and subsequent ϕ-gradients leads to local variations of the suspension viscosity (μ), due to the strong ϕ-dependence of μ. In the dense regime, even small changes in ϕ can cause significant changes in μ.

The distribution of solids in concentrated suspensions is further complicated in fully three-dimensional geometries such as fractures. Across the fracture aperture, the fluid will develop a solid distribution with higher concentrations towards the centerline. This non-uniform solid distribution will induce variation in the effective μ that lead to nonlinear velocity gradients across the gap. As for flow along the fracture, Medina et al. recently flowed a multimodal concentrated suspension (ϕ=0.5) through a transparent fracture and observed a strongly two-dimensional flow field within the fracture. They observed particles near the walls moving significantly faster than particles travelling in the middle of the fracture. The velocity variation within the fracture was attributed to variations in ϕ, across the plane of the fracture, which was subsequently confirmed through numerical simulations [10]. However, the source of such concentration gradients in the plane of the fracture was not fully identified in their experiments. The goal of the present work is to investigate the formation of ϕ-gradients perpendicular to the flow direction, along the fracture plane.

We present results from a set of four experiments in which we flowed a concentrated suspension (ϕ = 0.5) through the same parallel-sided fracture with different obstructions placed within the fracture. By varying the location and orientation of the obstruction we aimed to investigate the source of the previously observed ϕ variations [10]. The development of a ϕ-gradient would manifest itself through velocity fluctuations (i.e. a non-uniform velocity field), which we measure during experiments using optical techniques. We focus on conditions where suspended solids flow with the fluid, and we do not explore the regime where settling of solids within the fracture is important.

2. EXPERIMENTAL SETUP

To explore the role of concentrated suspension rheology and fracture geometry we used an experimental apparatus that allows quantitative visualization of the entire flow field [10]. Here we briefly describe the experimental apparatus, the details of the fluid-solid mixture, and the procedure used to carry out the experiments.

2.1. Experimental Apparatus

A rotating stand rigidly mounts a high-sensitivity charge-coupled device (CCD) camera (Photometrics Quantix KAF-6303e) above a monochromatic (red) LED panel (Fig. 1). Clamps secure the fracture cell to the stand between the light source and the camera. The fracture cell secures the fracture plates with a fixed space between the surfaces and allows light transmission through the entire flow field. The fracture surfaces (15 cm × 15 cm × 1.2 cm smooth glass plates) are separated by two aluminum shims which act as no-flow boundaries along the fracture edges and provide a uniform fracture aperture of ~0.3 cm. Two 2.5 cm-thick fused-quartz windows supported by 2.5 cm-thick aluminum frames clamp the fracture surfaces together (Fig. 1). An electronic controller synchronizes 65 ms pulses of the LED panel with exposure of the CCD to provide reproducible images of the fracture. The CCD camera uses 12-bit digitization of the measured intensities in images with a resolution of 76 μm per pixel.

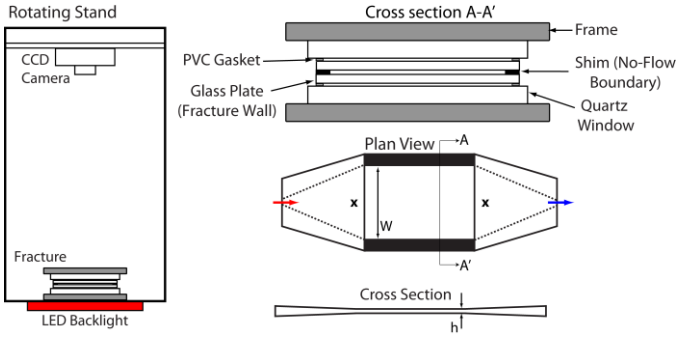

Fig. 1. (*left*) Schematic of rotating stand housing the fracture, LED panel, CCD camera, and controllers (not shown). (*right*) Transparent parallel-plate fracture and manifold configuration. The manifold gradually tapers from the inlet/outlet tubing to the fracture geometry. Schematic shows the location of the inlet (red arrow), outlet (blue arrow), and pressure ports (black cross), which are connected to the differential pressure transducer.

We carried out four experiments in the same parallel-plate fracture, changing the location and orientation of obstructions between experiments. The inlet/outlet manifolds were wedge-shaped and tapered gradually from the inlet port (red arrow) to a slot with the same width (W) and aperture (h) as the fracture (Fig. 1). A differential pressure transducer connected to the ports located at the center of the inlet and outlet manifolds (marked by Xs in Fig. 1) measured the differential fluid pressure across the fracture at a frequency of 0.3 Hz during each experiment. The cell in Experiment A did not include any obstructions within the fracture (Fig. 2a). A thin obstruction was placed in the middle of the fracture in Experiment B. The obstruction was 10 cm long, spanning 2/3 the length of the fracture and was oriented parallel to the flow (Fig. 2b). Experiment C included the same obstruction used in Experiment B oriented at an angle of approximately 5 degrees; the obstruction was centered along the x-axis and shifted off-center in the y direction (Fig. 2c). The leading edge of the obstruction in Experiment C was offset ~3 cm away from the wall of the no-flow boundary to avoid interruption of the high velocity region described by Medina et al. [10]. Experiment D included two obstructions placed symmetrically off the centerline of the fracture at a steep angle of approximately 27 degrees (Fig. 2d) with ~2 cm clearance between the trailing edge

of the obstruction and the wall. The leading edges of all obstructions were sharp, as seen on Fig. 2e, to reduce the potential of developing a stagnation zone or jamming.

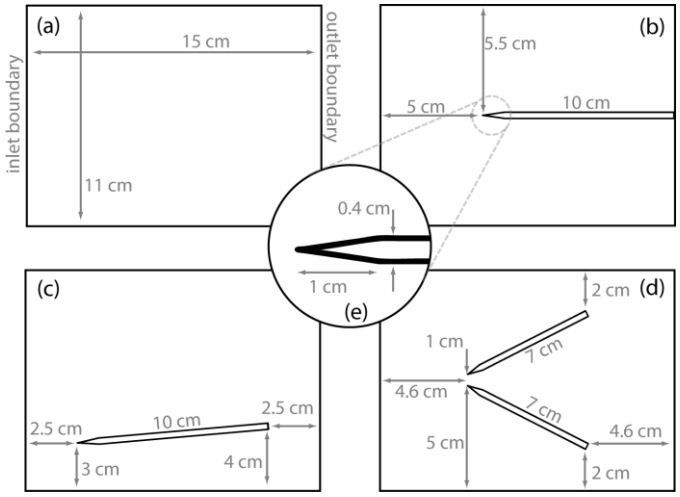

Fig. 2. Schematic showing the location and orientation of obstructions within the fracture for the four different experiments: (a) no obstruction, (b) horizontal obstruction, (c) single obstruction at a shallow (5 degree) angle, and (d) two obstructions at a steep (27 degree) angle. The insert (e) shows detail of the leading edge of the obstructions. In all experiments flow is from left to right.

2.2. Procedure for Flow Through Experiments

The concentrated suspensions were composed of a mixture of guar gum (a high viscosity, shear-thinning fluid) and silica sand. All experiments used a mixture of 0.75% (w/w) guar gum and water as the base (carrier) fluid. A laboratory-grade blender (Waring 7012g) mixed the guar/water solution for at least 10 minutes to ensure complete hydration of the guar. The fluid was then placed under vacuum for approximately 12 hours to remove any air bubbles entrapped during mixing and further enhance the hydration process.

We prepared the concentrated suspension by adding 50% (v/v) silica sand to the de-aired carrier fluid. The sand had a multimodal size distribution with three distinct nominal particle diameters of 352 μm, 46 μm, and 3 μm (particle size ratio 117:15:1). The full particle size distribution included grains as small as several microns with the largest grains ~600 μm. A rotary mixing paddle mixed the slurry as we slowly added sand to the carrier fluid. A lid with a vacuum-tight pass-through for the mixing paddle sealed the container, and the paddle mixed the slurry under vacuum for approximately 15 minutes to ensure a well-mixed and de-aired concentrated suspension.

We minimized solids settling by transferring the concentrated suspension into a syringe pump and beginning the flow-through experiment immediately after mixing. The syringe pump consisted of a clear polycarbonate pipe (1.7 m long, 2.5 cm inner diameter) fitted with a plunger from a 60-ml syringe. A plastic funnel secured to the bottom of the pipe provided a smooth transition from the 2.5-cm inner-diameter pipe to 8-mm inner-diameter tubing. Water pumped into the opposite end of the polycarbonate pipe at specified flow rates displaced the plunger and pushed slurry through the funnel and into the fracture.

Flow experiments involved the following steps: (1) filling the inlet tubing with carrier fluid while taking care to avoid introducing air bubbles that could induce optical artifacts; (2) slowly filling the fracture with carrier fluid and acquiring reference images; (3) connecting the tube carrying the slurry from the syringe/funnel to the inlet port on the manifold and rotating the fracture orientation to horizontal; (4) initiating image and data acquisition and flow of the concentrated suspension at a flow rate of 6.0 ml min^{-1}; (5) increasing the light intensity when the fracture was uniformly filled with the concentrated suspension to enhance image resolution; and (6) initiating the stepped flow-rate experiment.

3. IMAGE ANALYSIS

Images captured with the CCD camera measured light-intensity values which were later converted to light absorbance. Using absorbance allows quantitative comparison of images between experiments by eliminating the influence of small variations in light-source intensity. Additionally, absorbance fields provide greater contrast between flowing particles and the carrier fluid. Preprocessing of images corrected small registration errors and variations in emitted light intensity [11].

3.1. Aperture Measurement

Though the fracture consisted of two glass plates, small long-wavelength variations or small defects in the glass are common. Light transmission techniques were used to measure the fracture aperture field. Light absorbance is related to light intensity by applying the Beer-Lambert law to measurements of the fracture filled with clear and dyed water:

$$A_{i,j} = \ln\left(\frac{I_{clear\ i,j}}{I_{dye_{i,j}}}\right)$$

where A is the absorbance at a point (i,j), I_{clear} and I_{dye} are measured light intensity of the fracture filled with clear and dyed water, respectively. The mean fracture aperture was measured by injecting a known volume of fluid into the fracture and calculating the area occupied by the fluid, a detailed procedure can be found in Medina et al. [10]. The spatial distribution of aperture within the fracture is then given by [11]:

$$h_{i,j} = \frac{A_{i,j}}{\langle A \rangle}\langle h \rangle$$

where h is the fracture aperture, A is the absorbance, and $\langle\ \ \rangle$ represents spatial averaging. The measured average aperture, $\langle h \rangle$, for all the experiments was ~3450 μm. Measurements also revealed a small (long-wavelength) spatial variation of approximately 50 μm, with the regions near the no-flow boundaries having the smallest aperture.

3.2. Particle Image Velocimetry

Particle image velocimetry (PIV) analysis was performed using a modified version of the Matlab-based software, PIVlab [12]. A high-pass filter applied to the absorbance fields removed long wavelength features and increased contrast between individual sand grains and the surrounding carrier fluid. The fracture image was divided into 32×32 pixel sub-regions and the cross-correlation was then calculated for co-located sub-regions between two consecutive images. PIV analysis provides a measure of the average solids displacement within each sub-region from one frame to the next. We performed PIV analysis on the entire dataset (thousands of images) to construct a time-series of the velocity field within the fracture.

4. EXPERIMENTAL RESULTS

The fracture and all associated tubing were initially filled with carrier fluid as explained in Sec. 2.2, which allowed acquisition of a reference image. The experiments were initialized by injecting concentrated suspension at a flow rate of 6 ml min^{-1}, which allowed us to fill the fracture and tubing with concentrated suspension in a relatively short time. After the system was filled with slurry, the light intensity was increased to enhance image resolution. All experiments were carried out by decreasing the flow rate through a sequence of steps (Q = 3, 1.5, 0.8, 0.4, 0.2 ml min^{-1}, in that order); the flow was then increased through a subset of the same flow rates (Q = 0.4, 0.8, 1.5, 3 ml min^{-1}). The flow was allowed to reach quasi steady-state at each flow rate, as measured by the pressure differential and effluent mass-flow-rate.

Figure 3 shows the time series plot of measured pressure difference and effluent flow rate throughout the duration of Experiment D. The time series for all experiments shows similar trends, however, for clarity we only present the time series data for one experiment. The data for all experiments reveals a transient ΔP in response to each instantaneous change in inflow rate (Q_{in}). With each change in Q_{in} the outflow rate (Q_{out}), reached the value of Q_{in} after a short delay (t_{flow}). We also observed a large change in ΔP (shown in the plot as a dip or peak for decreasing and increasing flow rates, respectively) followed by a much slower partial recovery of ΔP. The timescale associated with the initial large change in ΔP corresponds to the timescale of the change in flow rate (t_{flow}).

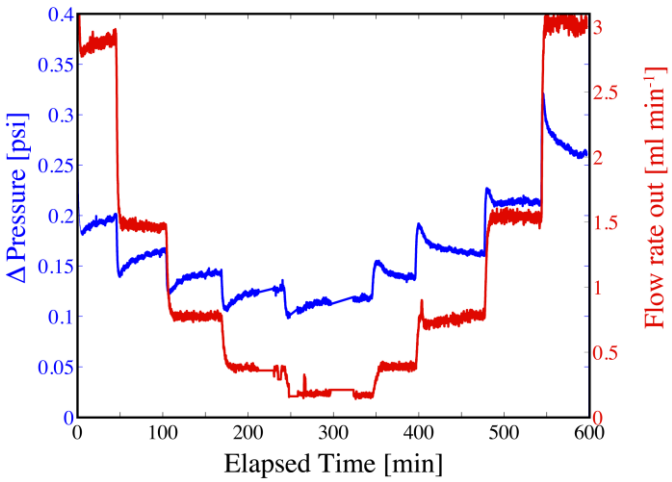

Fig. 3. Time series showing pressure differential across the fracture and flow rate for Experiment D. Time zero is immediately after flow rate was decreased from 6 ml min^{-1} to 3 ml min^{-1}. The pressure response shows a transient behavior at every step change in flow rate.

PIV analysis provides discrete measurements of the velocity within the fracture. Averaging sequential velocity fields measured during a period when the observed flow rate was approximately constant (at the end of each flow rate step) provides a relatively noise-free measure of velocity throughout the fracture at each flow rate. Figure 4 shows a representative subset of these velocity fields for the decreasing flow rate sequence for all experiments. To compare the results between experiments, we normalized the velocity fields by the average fluid velocity, $\langle V \rangle = \frac{Q_{out}}{W\langle h \rangle}$. During Experiment A, the flow field was nearly one dimensional throughout the duration of the experiment. However, we observed that the highest velocities occurred along the no flow boundaries (top and bottom of each frame in Fig. 4), where one would normally expect the velocity to be lowest due to the no-slip condition at the boundaries (as reported earlier in [10]). These high-velocity regions are ~2 cm in width and have an average velocity ~2.5 times higher than the mean velocity within the fracture. These high-velocity regions developed at early times and persist at all flow rates, however, their width increases with decreasing flow rate as can be observed in the first row of Fig. 4. As previously discussed [10], the most likely cause for these high velocity bands is a slight variation of ϕ within the fracture. Through numerical simulations, Medina et al. showed that a small decrease in solid concentration in these regions ($\phi = 0.5 \rightarrow 0.47$) could explain a large velocity increase, up to twice the average velocity, consistent with the experiments presented here. Additionally, we observed a slight increase in velocity (relative to the mean velocity) at the lowest flow rate for Experiment A. While the cause of this velocity increase is not fully understood, we offer three possible explanations. It is possible for suspended solids to travel faster than the

bulk fluid in concentrated suspensions, especially in the centerline where concentration is highest. The second possibility is that as $Q \rightarrow 0$ some solids might settle inside the fracture and form a sub-layer; thus, the concentrated suspension moves through a reduced aperture. The third possibility is that we are sampling the transient state of the flow (i.e., ΔP is still changing) and, thus, it is possible that the solids velocity is not yet fully developed for each flow rate.

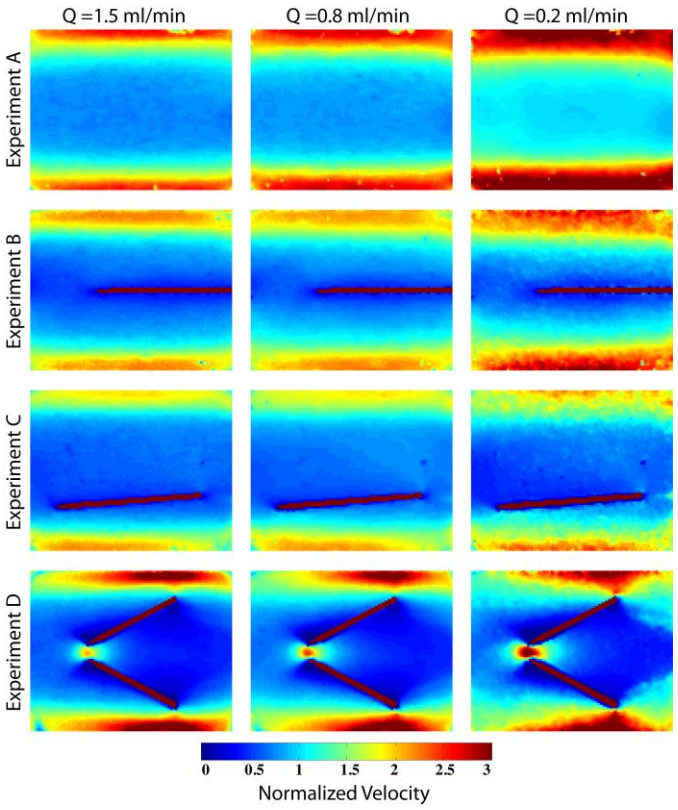

Fig. 4. Normalized velocity field for a subset of flow rates taken during the step-down part for all experiments. The velocity is normalized by the average velocity $\langle V \rangle = Q_{out}/(W\langle h \rangle)$ at each flow rate. A high velocity region near the no-flow boundaries (top and bottom of each frame) is persistent for all experiments at all flow rates.

From Experiment A, we hypothesized that the no-flow boundaries cannot create shear gradients large enough to cause ϕ-variations (~2 cm wide) in the plane of the fracture. Placing obstructions within the fracture allowed us to test whether a no-slip boundary within the fracture would develop such concentration gradients. Experiments B and C showed similar behavior to that of Experiment A: high velocity bands develop near the no-flow boundaries at early times and persist throughout the experiments. However, the PIV analysis shows that the obstruction decreases the velocity of the region immediately adjacent to it. This is more clearly depicted in Figure 5 which plots the velocity vectors for Q= 0.2 ml min^{-1}. The obstructions disrupt the velocity of a region of approximately 1-2 vectors (in the horizontal direction) which corresponds to ~32-48 pixels (2.4-3.6 mm), i.e., the same order of magnitude as the mean aperture $\langle h \rangle = 3450\ \mu$m. The stark contrast in velocity behavior at the no-flow boundaries and obstructions (both no-slip boundaries) supports the idea that the high-velocity regions developed outside of the fracture.

The velocity field for Experiment D shows a similar trend with high velocity near the no-flow boundaries. However, unlike the previous experiments, Experiment D includes two stagnation points at each of the obstructions: one on the outside at the leading edge and one on the inside at the trailing edge. These stagnation points caused the velocity of solids near these regions to drop to zero creating small, localized jammed regions though most of the flow remains unaffected by these jammed regions. The PIV analysis also shows that, in Experiment D, the normalized velocity of the flowing regions increases, notably in the small constriction between the obstructions. The velocity field for Experiment D also shows the interesting result of the high velocity zones near the no-flow boundaries changing shape as we decrease the flow rate, where they expand to reach the trailing edge of the obstruction.

5. DISCUSSION

The pressure differential plot (Fig. 3) suggests that the flow is in a transient state for all flow rates during each of the experiments. For concentrated suspensions there are two different timescales that must be considered: 1) the timescale associated with the flow rate equilibration (t_{flow}) and 2) the time it takes to reach fully developed flow (t_{dev}), or the time required for the distribution of solids to reorganize after a change in the local shear stresses (caused by a change in flow rate). As previously discussed, t_{flow} is the time it takes for Q_{out} to equilibrate with Q_{in}; this time is relatively short, on the order of ~2-3 minutes for our experiments, and reflects elasticity in the plumbing and small amounts of entrapped air in the syringe pump. The sharp decrease/increase observed in pressure after changing the flow rate coincides with t_{flow}; however, the transient ΔP behavior persisted well after the flow rates reached steady state. The development time (t_{dev}) is the time it takes the suspension to reach a fully-developed state, which happens at a distance (L_{dev}) away from the inlet of the tube; this distance is the characteristic length associated with particle re-arrangement. Even if the solids are uniformly distributed when they enter the tube, shear gradients cause solids to migrate towards the centerline of the tube creating a blunted solid distribution [13, 14]; this particle migration ceases once the flow reaches a fully developed state at a distance, L_{dev}.

The development time is given by $t_{dev} = h^2/(4D)$, where D is the self-induced shear-diffusion ($D = d(\phi)\dot{\gamma}a^2$), $d(\phi)$ is the diffusion coefficient, $\dot{\gamma}$ is the

effective shear rate (approximated as $\langle V \rangle/(h/2)$ for this scaling analysis), and a is the particle radius [15]. Converting the t_{dev} to a length scale yields $L_{dev} = \frac{1}{8d(\phi)}\frac{h^3}{a^2}$. For concentrated suspensions, the diffusion coefficient can be approximated by $d(\phi) = \frac{1}{3}\phi^2\left(1 + \frac{1}{2}e^{8.8\phi}\right)$ [16]. For our experiment, the tube radius is R=0.4 cm (equivalent to h in the equation for L_{dev}). If we then assume uniform solid content of $\phi_0 = 0.5$ at the inlet and a particle diameter of ~352 μm, we estimate $d(\phi_0) = 3.5$ and $L_{dev} \approx 12.5$ cm. The tube connecting the syringe pump to the inlet manifold was approximately 2 m long; additionally, the duration of each flow rate (~40~80 minutes, with lower flow rates having largest time of flow) was larger than this estimated development time, suggesting that the flow entering the manifold was fully developed. However, once the flow enters the manifold, the solids must re-arrange as the geometry expands and then adjust again as they enter the fracture. In the fracture, the development length scales with fracture aperture $\propto h^3$ instead of R^3, i.e. $L_{dev} \approx 4.5$ cm. This suggests that the flow becomes fully developed within the fracture. The timescales associated with these development lengths for our experiments range from t_{dev}=45 minutes for the lowest flow rates to t_{dev}=3 minutes at the highest flow rates. However, the transient behavior observed in our measurements of ΔP occurs over somewhat longer timescales than predicted using this simple scaling analysis. In addition, the experimentally observed pressure transients exhibit only a weak dependence on the flow rate, which deviates from predictions. Possible causes for these discrepancies between observations and theoretical predictions include three-dimensional effects due to the expanding geometry in the manifolds, additional shear-diffusion across the width of the fracture (i.e. particle re-arrangement in the plane of the fracture), and the non-Newtonian, shear-thinning nature of the carrier fluid.

A ϕ-gradient across the gap or along the plane of the fracture will cause a strongly non-uniform velocity field [13, 14]. For example, the high velocity regions (top and bottom of frames in Fig. 4) observed in all experiments are indicative of a ϕ-gradient in the plane of the fracture. A quantitative analysis of the velocity field can thus be used to infer a non-uniform solid distribution. In Experiment A, we observed that the high velocity regions form outside the fracture and propagate into and through the fracture. The placement and orientation of obstructions in experiments (B-D) were chosen to investigate the development of non-uniform velocity adjacent to no-flow boundaries within a fully developed region of the flow. High velocity regions next to the obstruction would indicate the development of a ϕ-gradient. Results for Experiments B and C show no significant velocity increase in the region adjacent to the obstructions with a shallow angle (0 and 5 degrees, respectively). Note that we also observe an increase in relative velocity along the fracture no-flow boundaries as we decreased the flow rate. This relative velocity increase might be explained by the mechanisms previously described in Section 4.

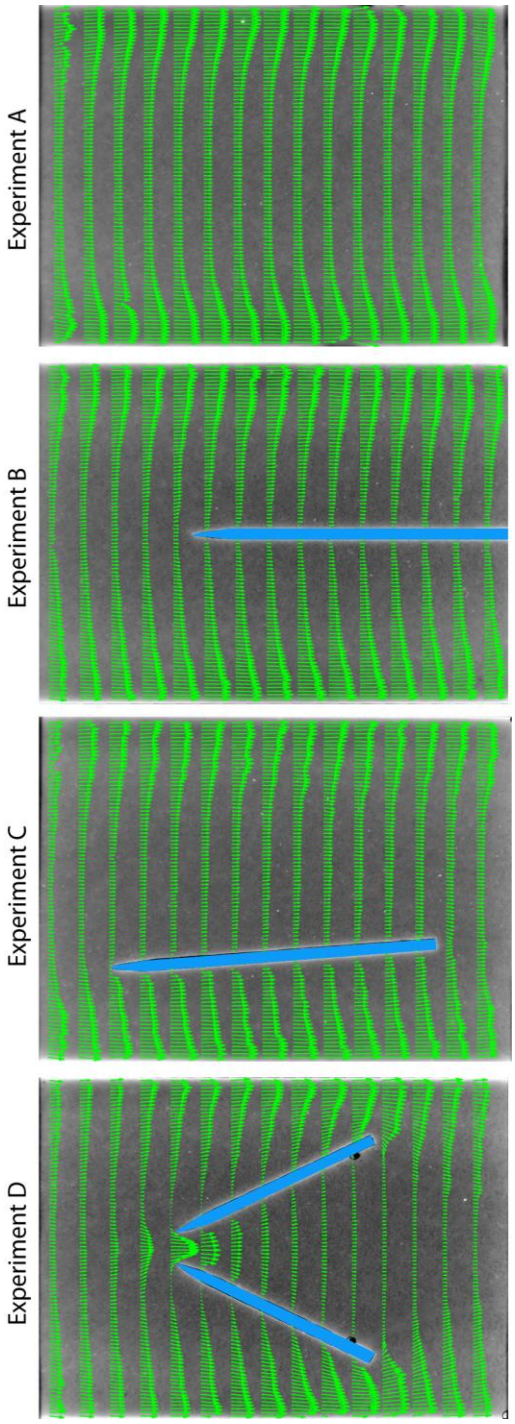

Fig. 5. Gray-scale image of the absorbance fields for all experiments at a flow rate of 0.2 ml min^{-1}. The green arrows represent the velocity magnitude at the region where the arrow originates. For clarity, we included all velocity vectors in the vertical direction (across the fracture), but only include every 8th vector in the direction of the flow and highlight the location of the obstructions in blue.

The angle and position of the obstructions in Experiment D were chosen to replicate the manifold configuration within the fracture. There are no strong velocity variations along the obstructions. Along the fracture no-flow boundaries, the relative velocity increases as the flow rate decreases following the trend observed in previous experiments. For Experiment D, the high velocity regions do not grow uniformly, as is the case for previous experiments. As flow rate decreases, the change in velocity under the leading edge of the obstruction is not as significant as the change in velocity at the trailing edge of the obstruction. However, between the two obstructions, the velocity field only varies at the narrow constriction (entrance) with no significant velocity gradients observed elsewhere in this region. This indicates that the manifold geometry by itself is not enough to create the ϕ-gradients observed along the fracture no-flow boundaries.

6. CONCLUSION

We have shown that gradients in solid volume fraction (ϕ) introduced at the inlet of our experimental system persist through the fracture and have significant effects on the velocity field. High velocity regions observed near the fracture no-flow boundaries are not observed along the edges of obstructions placed within the fracture. While the strong velocity gradient within the fracture is indicative of a ϕ-gradient, we showed that these gradients were pre-existing by the time the concentrated suspension entered the fracture. The results indicate that fully developed suspension flow that transitions into a larger geometry, such as a fracture, further complicates the development of non-uniform solid distribution in the plane of the fracture. Though we did not observe the development of concentration gradients within the fracture (in the direction normal to the obstructions), we observed a pronounced transient behavior in the pressure drop across the fracture. This transient behavior can have large implications, when designing experiments or interpreting pressure data from field operations, as the timescale for development of a steady pressure response might be orders of magnitude larger than expected.

REFERENCES

1. Mueller, S., E., W. Llewellinand, and, H. M. Mader. 2009. The rheology of suspensions of solid particles. *Proceedings of the Royal Society A: Mathematical, Physical and Engineering Science.*
2. Kern, L. R., T. K. Perkins, and R. E. Wyant. 1959. The Mechanics of Sand Movement in Fracturing: *Transactions of the American Institute of Mining and Metallurgical Engineers* 216: 403–405.
3. Montgomery, C. 2013. Fracturing Fluids, Effective and Sustainable Hydraulic Fracturing. A. P. Bunger, J. McLennan and R. Jeffrey (Ed.), ISBN: 978-953-51-1137-5, InTech, DOI: 10.5772/56192.
4. Murdoch, L. C., J. R. Richardson, Q. F. Tan, S. C. Malin and C. Fairbanks, C. 2006. Forms and sand transport in shallow hydraulic fractures in residual soil. *Canadian Geotechnical Journal* 43 (10): 1061–1073.
5. Lecampion, B., and D. Garagash. 2014. Confined flow of suspensions modeled by a frictional rheology. *J. Fluid Mech.* 759: 197-235.
6. Deboeuf, A., G. Gauthier, J. Martin, Y. Yurkovetsky, and J. F. Morris. 2009. Particle Pressure in a Sheared Suspension: A Bridge from Osmosis to Granular Dilatancy. Physical Review Letters 102 (10): 108301-1–108301-4.
7. Boyer, F., E. Guazzelli, and O. Pouliquen. 2011. Unifying Suspension and Granular Rheology. *Physical Review Letters* 107 (18): 188301-1–188301-5.
8. Shapiro, A. P. and R. F. Probstein. 1992. Random packing of spheres and fluidity limits of monodisperse and bidisperse suspensions. J. Phys. Rev. Lett. 68: 1422-1425.
9. Leighton, D., and A. Acrivos. 1987. The shear-induced migration of particles in concentrated suspensions. *J. Fluid Mech.* 181: 415-439.
10. Medina, R., J. E. Elkhoury, J. P. Morris, R. Prioul, J. Desroches, and R. L. Detwiler. 2015. Flow of concentrated suspensions through fractures: small variations in solid concentration cause significant in-plane velocity variations. *Geofluids* 15 (1-2): 24-36.
11. Detwiler, R. L., S. E. Pringle, and R. J. Glass. 1999. Measurement of fracture aperture fields using transmitted light: An evaluation of measurement errors and their influence on simulations of flow and transport through a single fracture: *Water Resources Research* 35 (9): 2605–2617.
12. Thielicke, W., and E. Stamuis. 2012. PIVLab: Time-resolved digital particle image velocimetry tool for MATLAB. Ver. 1.32. http://pivlab.blogspot.com/.
13. Oh, S., Y. Song, D. Garagash, B. Lecampion, and J. Desroches, 2015. Pressure-driven suspension flow near jamming. Phys. Rev. Lett. 114 (8): 088301.
14. Eskin, D. and M. J. Miller. 2008. A model of non-Newtonian slurry flow in a fracture. Powder Technology 182 (2): 313 – 322.
15. Nott, P.R. and J.F. Brady. 1994. Pressure-driven flow of suspensions: simulation and theory. J. Fluid Mech. 275: 157-199.
16. Leighton, D. and A. Acrivos. 1986. Viscous Resuspension. Chemical Engineering Science 14 (2): 1377 – 1384.